Facies-based FWI for anisotropic media: A North Sea case study

Sagar Singh[*], Ilya Tsvankin[*], & Ehsan Zabihi Naeini[†]

[*] *Center for Wave Phenomena and Dept. of Geophysics, Colorado School of Mines, Golden CO 80401*
[†] *Earth Science Analytics, London*
email: sagarsingh@mines.edu

ABSTRACT

Elastic full-waveform inversion (FWI) can substantially increase the resolution of reservoir characterization using seismic data. However, FWI for realistic anisotropic media suffers from the trade-offs between the medium parameters and strongly relies on the accuracy of the initial model. Here, we employ a regularization methodology that utilizes geologically consistent information to reduce the inversion nonlinearity and crosstalk between the parameters. The geologic constraints are obtained from well logs and interpolated along major horizons in the migrated image. The algorithm, designed for transversely isotropic media with a tilted symmetry axis (TTI) is applied to ocean-bottom data acquired at Volve field in the North Sea. The facies-based constraints help build high-resolution velocity fields and accurately image the reservoir region. In particular, the developed algorithm substantially increases the resolution of the P- and S-wave symmetry-direction velocities and other parameters at the reservoir level. The facies-based FWI also provides robust estimates of density, which is inverted simultaneously with the velocity fields. Overall, even relatively sparse prior information proves to be sufficient for the proposed methodology to achieve a much higher spatial resolution than the unconstrained FWI.

Key words: Tilted TI media, Volve data, elastic FWI

1 INTRODUCTION

Full-waveform inversion (FWI) has the potential of delivering high-resolution velocity models of complex geologic structures (Tarantola, 1984) and providing accurate estimates of the reservoir properties. However, implementing FWI for realistic elastic anisotropic reservoir models is a computationally challenging task (e.g, Singh et al., 2020a,b). Furthermore, the crosstalk between the parameters of anisotropic media and the insufficient quality of the initial model often hamper the convergence of model updating.

Crosstalk or trade-off occurs when the data residuals caused by an error in one physical property or parameter are attributed to another parameter, impeding the updating procedure and possibly leading to geologically inconsistent features in the inverted models. Analyzing radiation (scattering) patterns of the medium parameters can yield valuable insights into potential trade-offs and the types of input data required for reliable parameter estimation. Such sensitivity analysis is especially valuable for anisotropic media (Alkhalifah and Plessix, 2014; Kamath and Tsvankin, 2016; Singh and Tsvankin, 2021). Trade-offs can also be mitigated by Newton-based optimization methods that utilize the inverse Hessian matrix (Operto et al., 2013; Pan et al., 2016).

Because FWI is a local optimization algorithm, it is sensitive to the choice of the initial model, which needs to be sufficiently close to the actual model. Due to the inherent nonlinearity of FWI, the objective function usually contains local minima, which can prevent convergence toward the actual parameters, if the initial model is inaccurate. Inversion of ultra-low frequencies (0-2 Hz) can yield an adequate background model but such frequencies are seldom acquired in typical seismic surveys. Li and Demanet (2016) propose synthesizing ultra-low frequency data by extrapolating seismic records, which may allow FWI to build kinematically accurate models. Wu et al. (2014) employ a demodulation operator to obtain the long-wavelength model, which is then used for high-frequency FWI updates.

Constraining the model-updating procedure by incorporating prior information about the subsurface (e.g., geologic facies)

has proven promising in mitigating the problems mentioned above (Guitton et al., 2012; Asnaashari et al., 2013; Singh et al., 2018, Zhang at al., 2018; Singh et al., 2020b). The primary source of this geologic information is available well logs. However, the sparseness of borehole locations makes it difficult to account for realistic lateral heterogeneity. An image-guided interpolation technique (Zabihi Naeini and Hale, 2015) or machine-learning networks (Singh et al., 2020c; Zhang and Alkhalifah, 2019, 2020) have been proposed to build the spatial distribution of the constraints for laterally heterogeneous media.

Here, we apply to ocean-bottom data (a 2D line from Volve field in the North Sea) a modified version of the FWI algorithm developed by Singh et al. (2020b) for VTI (transversely isotropic with a vertical symmetry axis) media. Their FWI methodology includes facies information as a regularization term in the objective function and employs the l^2-norm for simultaneous multi-parameter inversion. However, here we use a global-correlation-based objective function (Choi and Alkhalifah, 2012), which is more suitable for field-data applications. The objective function based on cross-correlation is sensitive to the similarity between the synthetic and recorded data. Because this objective function mostly matches the phase in seismic traces, it is less influenced by the amplitude correspondence required by the l^2-norm. The cross-correlation approach, equivalent to phase inversion in the time domain (Dutta et al., 2014), is particularly useful for field-data applications, where amplitude matching is problematic.

Zhang and Alkhalifah (2020) perform FWI for the same 2D line at Volve field using facies information derived from a convolutional neural network. However, they assume the medium to be VTI (i.e., they do not take the symmetry-axis tilt into account) and employ a hierarchical parameterization (Jarillo Michel and Tsvankin, 2017), which proves to be suboptimal in delineating the reservoir region.

The results of reflection tomography for this Volve-field line (Wang and Tsvankin, 2013) show that taking the tilt of the symmetry axis into account substantially improves migrated images. Therefore, here we perform FWI for tilted TI media with the axis orientation estimated from the structural dips. Also, we employ a velocity-based parameterization, shown to be particularly effective in facies-constrained FWI (Singh et al., 2018; Singh et al., 2020b).

Each geologic facies considered in the case study occupies a certain horizon identified from a migrated image. The logs from the available boreholes are assigned to each facies, and the spatial distribution of the elastic properties is built by interpolating the borehole information along the major horizons in the image. The image-guided elastic properties are then calibrated with the facies and borehole data and used as a constraint in the inversion workflow.

In most existing FWI algorithms density is either assumed to be constant or computed from empirical relationships (e.g., Shipp and Singh, 2002; Brossier et al., 2009; Qu et al., 2017; Zhang and Alkhalifah, 2020). However, density is a crucial physical parameter in reservoir characterization and lithologic interpretation. Also, an accurate density model is beneficial for the velocity inversion (Pratt and Smithyman, 2018; Singh et al., 2018, 2020b, 2021; Singh and Tsvankin, 2021). Therefore, here we invert for the 2D density field and update it independently of the other parameters with the corresponding inversion gradient.

We start by discussing the FWI workflow for elastic TTI media and the main issues that can cause deterioration in the inversion results. Then we describe the facies-based FWI methodology where the model constraints are obtained from the available well logs and migrated image. The algorithm is applied to the ocean-bottom data from Volve field in the North Sea provided by Statoil (now Equinor). The inversion is carried out for the vertical particle-velocity component with the initial model based on the results of reflection tomography. Comparison with the conventional (unconstrained) FWI demonstrates the ability of the lithologic information to improve the parameter-estimation results, especially in the reservoir region.

FWI METHODOLOGY FOR TILTED TRANSVERSELY ISOTROPIC MEDIA

Application of FWI in reservoir characterization requires taking elasticity and anisotropy into account. Here, we implement FWI for elastic TTI media often encountered in the subsurface (Tsvankin and Grechka, 2011; Tsvankin, 2012). Below we discuss the objective function, inversion gradients, and facies-based constraints used in our algorithm.

1.1   Objective function

To overcome the difficulties in amplitude matching for field data, we employ the normalized zero-lag cross-correlation objective function (Choi and Alkhalifah, 2012):

$$E_{\rm d}(\mathbf{m}) = -\sum_{\rm s=1}^{\rm n_s} \frac{\sum_{\rm r} \int_0^T \mathbf{d}^{\rm obs}\, \mathbf{d}^{\rm sim}(\mathbf{m})dt}{\sqrt{\sum_{\rm r} \int_0^T (\mathbf{d}^{\rm obs})^2 dt}\sqrt{\sum_{\rm r} \int_0^T (\mathbf{d}^{\rm sim})^2 dt}}$$

$$\equiv -\sum_{\rm s=1}^{\rm n_s} \overline{\mathbf{d}}^{\rm obs} * \overline{\mathbf{d}}(\mathbf{m})^{\rm sim} \,, \tag{1}$$

where $\overline{\mathbf{d}}^{\rm obs} = \mathbf{d}^{\rm obs}/||\mathbf{d}^{\rm obs}||$ denotes the normalized observed data, $\overline{\mathbf{d}}^{\rm sim} = \mathbf{d}^{\rm sim}/||\mathbf{d}^{\rm sim}||$ is the normalized data simulated for a certain trial model, n_s is the number of sources, r is the trace number, and T is total recording time.

The large number of independent parameters makes anisotropic FWI highly nonlinear, and the objective function often has multiple local minima. For such multimodal objective functions, the initial model must lie in the vicinity of the global minimum (i.e., in the basin of convergence).

We simulate the displacement field $\mathbf{u}$ for 2D heterogeneous TTI media using the elastic wave equation:

$$\rho\, \partial_t^2 u_j = \sigma_{ij,j} + F_i \,, \tag{2}$$

where i,j =1,2, ρ is the density, $\mathbf{F}$ is the body force per unit volume, and $\sigma_{ij,j}$ are the spatial derivatives of the stress tensor; summation over repeated indices is implied. According to Hooke's law, the stress tensor can be written as:

$$\sigma_{ij} = d_{ijkl}\Big[\frac{1}{2}(u_{k,l} + u_{l,k})\Big], \tag{3}$$

where d_{ijkl} is the stiffness tensor.

The tensor d_{ijkl} in 2D TTI media has six independent elements and can be related to the stiffness tensor c_{ijkl} in the corresponding VTI medium by the Bond transformation:

$$d_{ijkl} = R(\theta)\, c_{ijkl}\, R(\theta)^T, \tag{4}$$

where θ is the tilt of the symmetry axis away from the vertical and $R(\theta)$ is the rotation matrix (e.g., Oh et al., 2020). Explicit expressions for the nonzero elements of d_{ijkl} can be found in Appendix A.

1.2   Notation and inversion gradient

The 2D elastic TTI model is parameterized here by the P- and S-wave velocities in the symmetry-axis direction ($V_{\rm P0}$ and $V_{\rm S0}$), the P-wave velocity in the isotropy plane $V_{\rm hor,P} = V_{\rm P0}\sqrt{1+2\epsilon}$ (which becomes the horizontal velocity if the symmetry axis is vertical), and the velocity $V_{\rm nmo,P} = V_{\rm P0}\sqrt{1+2\delta}$ (ϵ and δ are the Thomsen parameters for the corresponding VTI model). Note that for a vertical symmetry axis $V_{\rm nmo,P}$ becomes the P-wave normal-moveout velocity from a horizontal reflector. These four parameters, the tilt of the symmetry axis, and density control the signatures of the P- and SV-waves in the vertical plane that contains the symmetry axis (Tsvankin, 2012).

Note that density, which plays an essential role in reservoir characterization, is estimated along with the velocities by our FWI algorithm (Singh et al., 2020b). The symmetry axis is assumed to be orthogonal to the interfaces and is computed from the structural dips in the migrated image (Wang and Tsvankin, 2013). The relationships between the velocities defined above and the stiffness coefficients d_{ijkl} are listed in Appendix A. The advantages of the velocity-based parameterization for FWI applications are discussed in Singh et al. (2020b,c) and Kamath and Tsvankin (2016).

The gradient of the objective function with respect to the model parameters is computed from the adjoint-state method (e.g., Kamath and Tsvankin, 2016):

$$\frac{\partial E(\mathbf{m})_{\rm d}}{\partial \mathbf{m}} = -\Big[\frac{\partial \mathbf{d}^{\rm sim}}{\partial \mathbf{m}}\Big]\, \mathbf{q} \,, \tag{5}$$

where $\mathbf{q} = (1/||\mathbf{d}^{\rm obs}||)\, [\mathbf{d}^{\rm obs}(\mathbf{d}^{\rm obs}\mathbf{d}^{\rm sim}) - \mathbf{d}^{\rm sim}]$ is the residual wavefield.

The exact expressions for the FWI gradient can be found in Appendix B. We carry out iterative parameter updating with the nonlinear conjugate-gradient algorithm (e.g., Hager and Zhang, 2006).

The wave equation 2 is solved using a forth-order (in space) and second-order (in time) finite-difference algorithm. We apply the convolutional PML (perfectly matched layers) absorbing boundary conditions on the sides of the model but the top represents a free surface. The wavefield is excited by a point explosive source. The source signal is a bandlimited spike (to avoid grid dispersion) with a central frequency of 9 Hz. As in Singh et al. (2020b), we apply the domain-decomposition method (Bohlen, 2002) to reduce computational cost.

Facies-based constraints for FWI

Following Singh et al. (2018, 2020b), Zheng et al. (2018), and Zhang and Alkhalifah (2020), the facies-based constraints are included in the inversion workflow by adding the corresponding term $[E_f(\mathbf{m})]$ to the objective function $E(\mathbf{m})$:

$$E(\mathbf{m}) = E_\mathrm{d}(\mathbf{m}) + \beta\, E_f(\mathbf{m}) \, , \tag{6}$$

where

$$E_f(\mathbf{m}) = ||\mathbf{W}_m\, (\mathbf{m}^\mathrm{inv} - \mathbf{m}^\mathrm{f})||^2. \tag{7}$$

Here, the vector $\mathbf{m}^\mathrm{f}$ represents the facies-based elastic constraints to be obtained from borehole information, $\mathbf{m}^\mathrm{inv}$ is the inverted model, β is a scaling factor which determines the relative contribution of prior information, and $\mathbf{W}_m$ is a model-weighting diagonal matrix designed to make the facies-based term dimensionless and to assign larger weights to data around borehole locations. The gradient of the objective function in equation 6 can be found as follows (Asnaashari et al., 2013):

$$\frac{\partial E(\mathbf{m})}{\partial \mathbf{m}} = -\left[\frac{\partial \mathbf{d}^\mathrm{sim}}{\partial \mathbf{m}}\right]\mathbf{q} + \beta\, \mathbf{W}_\mathrm{m}^T\, \mathbf{W}_\mathrm{m}(\mathbf{m}^\mathrm{inv} - \mathbf{m}^\mathrm{f}). \tag{8}$$

The first term $[E_\mathrm{d}(\mathbf{m})]$ in equation 6 represents the data misfit computed from the zero-lag cross-correlation norm (equation 1), whereas the second one $[E_f(\mathbf{m})]$ is the model misfit, which includes prior facies information. By referring to the output of the unconstrained FWI below, we mean the result of minimizing only the data misfit $E_\mathrm{d}(\mathbf{m})$ (i.e., $\beta = 0$).

Application to Volve data set

Volve field is a Middle Jurassic oil reservoir located offshore Norway in the southern part of the Viking Graben in the gas/condensate-rich Sleipner area. It is a small dome-shaped structure formed by the collapse of adjacent salt ridges. The system is bounded from the south, east, and north by faults mainly produced by salt tectonics.

Acquisition design

The 3D OBS survey was acquired using inline shooting geometry over a 12.3 x 6.8 km area of the field (Figure 1). The sail line is 12 km long with a shot interval of 25 m (50 m between the flips). The data are recorded using a cable (at a depth of about 92 m) containing 240 receivers separated by 25 m.

Equinor (then Statoil) preprocessed the vertical and horizontal particle-velocity components by applying noise suppression, multiple attenuation, and other standard steps described in Szydlik et al. (2007). Only the shots with (absolute) offsets less than 5000 m were kept for further processing. A 3D VTI velocity model was built by Equinor using a layer-stripping approach, with each interval updated using a combination of layer-based tomography and migration scanning. The parameter-estimation procedure was constrained by well data, such as compressional and shear sonic logs, check shots, etc. The P- and S-wave vertical velocities V_P0 and V_S0 and the anisotropy parameters ϵ and δ in each layer were updated by flattening common-image gathers, minimizing the misties between seismic and well data, codepthing the key horizons on PP and PS migrated sections, and incorporating compressional sonic logs (Szydlik et al., 2007).

Wang and Tsvankin (2013) apply reflection tomography to the vertical particle-velocity component from the 2D line recorded along y = 2.8 km (white vertical lines in Figure 1). Two adjacent source lines (y = 2.8 ± 0.025 km) provided 481 shots with a shot interval of 25 m. Wang and Tsvankin (2013) carry out parameter estimation for a TTI medium and show their images to be superior
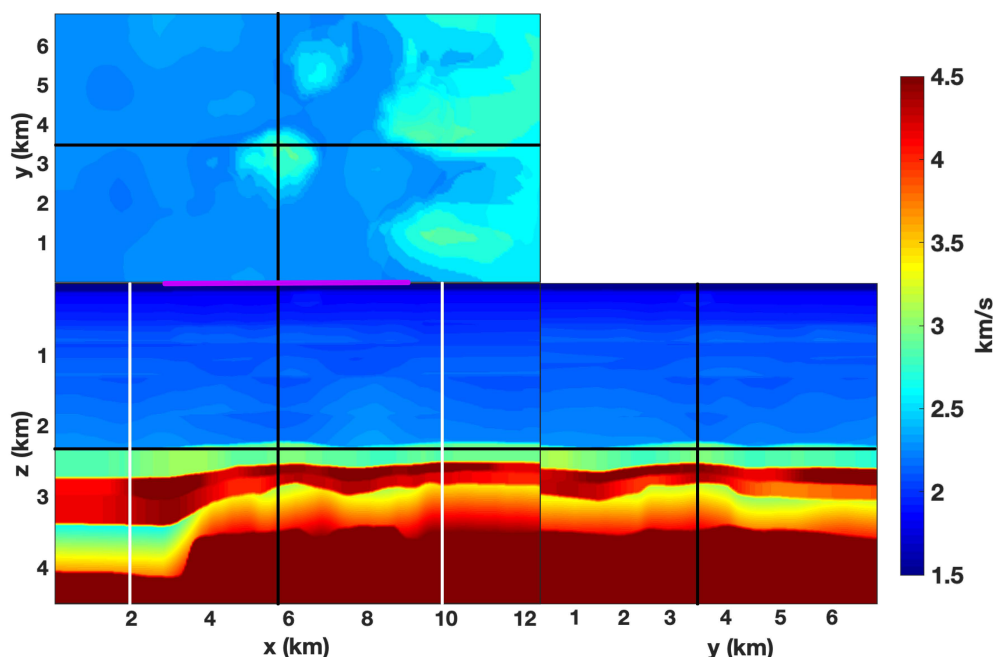
Figure 1. 3D tomography model for V_{P0} provided by Equinor. The cross-sections display the parameters in the coordinate planes at the center of the model. The area between the vertical white lines is used for 2D FWI. The horizontal magenta line on top of the $[x,z]$-section marks the source locations.

to those obtained by Equinor with a VTI model. Here, we apply FWI to the vertical-component data from the same line and also take the tilt of the symmetry axis into account. The inversion is performed for records from 118 shots placed along the magenta line in Figure 1.

FWI is constrained using borehole data from two deviated wells located near the chosen line (Figure 2). In addition to sonic (P- and S-waves) and density logs, the provided data also include the well markers (i.e., the depth measurements in the well) for several key horizons (e.g., the top and base of Utsira formation, top of Shetland Group, and bottom of Cretaceous layer).

Parameterization and initial model

As discussed above, the medium is parameterized by the P- and S-wave symmetry direction velocities (V_{P0} and V_{S0}), the P-wave velocity in the isotropy plane ($V_{hor,P}$), the NMO velocity ($V_{nmo,P}$), and density (ρ). Following Wang and Tsvankin (2013), the symmetry-axis tilt is estimated by computing the structural dips and setting the symmetry axis orthogonal to the interfaces. Because the tilt on this line is mild (up to $\pm 20°$), we recompute it only after every five inversion iterations.

The source wavelet and recorded data are filtered (2-15 Hz) before the inversion. To improve the convergence of the optimization method, we compensate for the amplitude decay with depth due to geometric spreading and multiple reflections in the overburden. This is achieved by preconditioning the FWI gradients using the inverse Hessian matrix obtained by the zero-lag correlation of the magnitude of the forward wavefield with an approximate receiver Green's function (Plessix and Mulder, 2004).

Because the horizontal particle-velocity component is severely contaminated with noise, only the vertical component is included in the inversion. The algorithm is designed to estimate the pertinent medium parameters (V_{P0}, V_{S0}, $V_{hor,P}$, $V_{nmo,P}$, and ρ) simultaneously using the inversion gradients listed in Appendix B. Note that the low frequencies in the 0-2 Hz range, which are absent in the recorded data, are filtered out from the simulated wavefield.

The initial velocity models (Figures 3e-h) represent 1D smoothed versions of the sections obtained by Equinor. The tomography models provided by Equinor in terms of the Thomsen parameters ϵ and δ were converted into the velocities $V_{hor,P}$ and $V_{nmo,P}$. Applying the same smoothing to the parameter fields obtained by Wang and Tsvankin (2013) produces similar results. The initial distribution of density (Figure 4) is computed from the initial velocity V_{P0} using Gardner's relationship for shale formations (Martin et al., 2006):
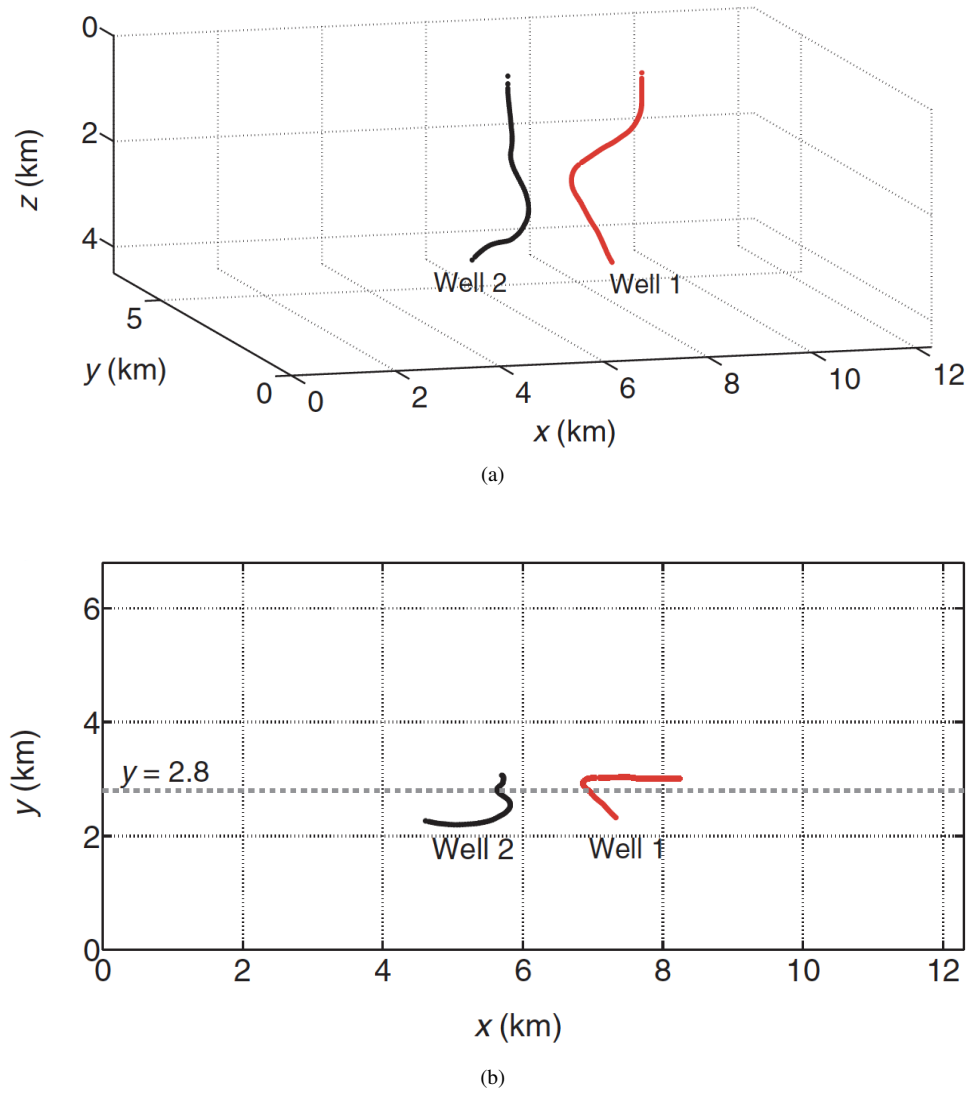
(a)

(b)

Figure 2. (a) Trajectories of two deviated wells near the line (y = 2.8 km, dashed) used in FWI. (b) The well projections onto the horizontal surface. The maximum deviations of the wells from the vertical plane at y = 2.8 km are 477 m and 603 m, respectively (adapted from Wang and Tsvankin, 2013).

$$\rho = 0.2806\, V_{\mathrm{P0}}^{0.265}. \tag{9}$$

The density in the water is set to 1 g/cm^3. Note that equation 9 is used only to compute the initial density model, which is updated independently during FWI using the corresponding inversion gradient.

1.3   Unconstrained FWI

The output of FWI without facies-based constraints is shown in Figure 5a-d. The inversion was performed for all shots in one frequency band (2–15 Hz). The inverted models contain more information about the subsurface velocity fields than the initial parameter distributions. In particular, there is a low-velocity (V_{P0}) layer at a depth of 3.1 km that likely represents the reservoir (Szydlik et al., 2007).

As shown in Singh and Tsvankin (2021), the vertical component may not be sufficiently sensitive to some elastic parameters
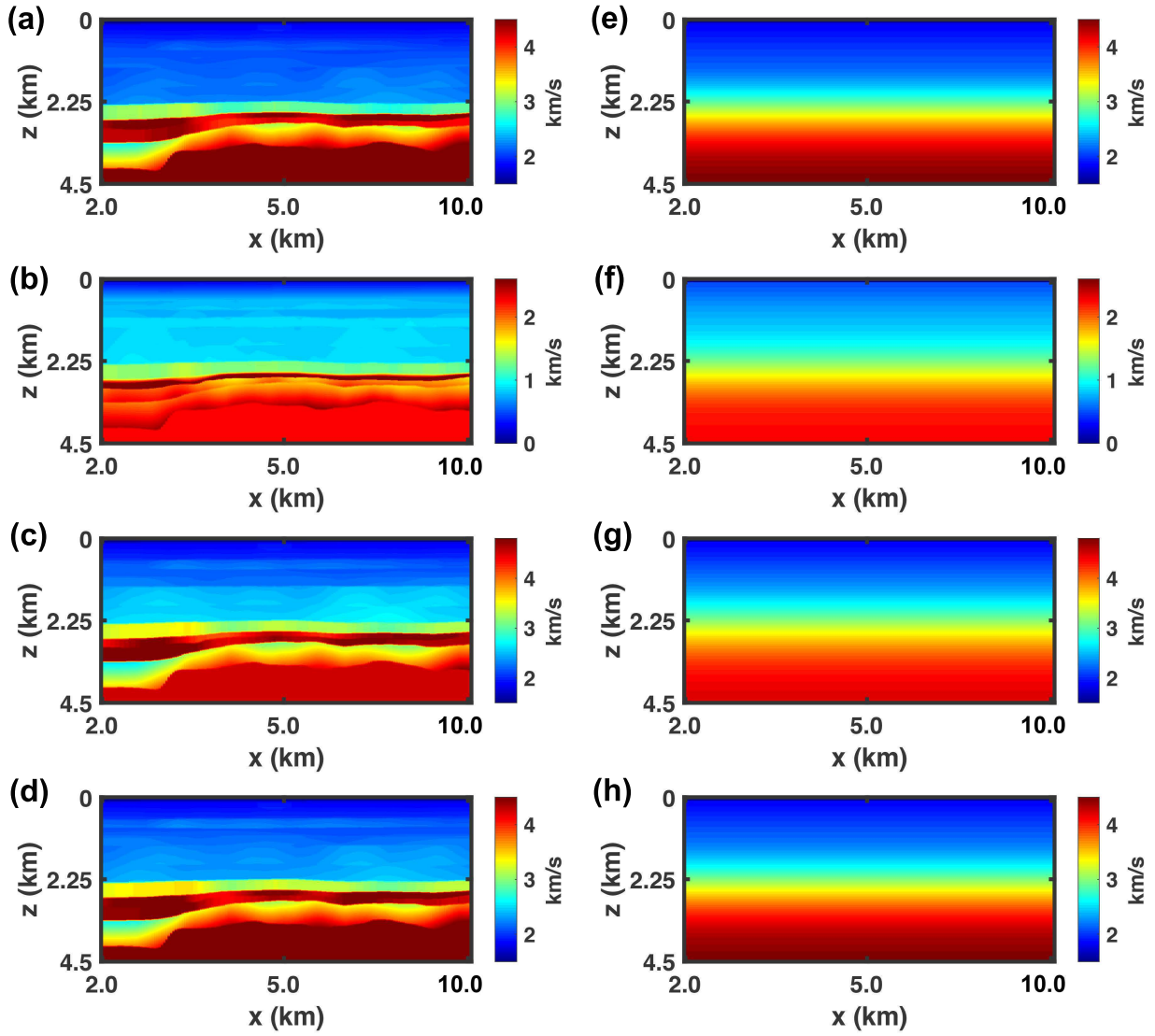
Figure 3. TI parameters extracted from the 3D tomography models provided by Equinor: (a) P-wave vertical velocity $V_{\mathrm{P}0}$, (b) S-wave vertical velocity $V_{\mathrm{S}0}$, (c) P-wave horizontal velocity $V_{\mathrm{hor,P}}$, and (d) P-wave NMO velocity $V_{\mathrm{nmo,P}}$. The initial parameters for FWI: (e) $V_{\mathrm{P}0}$, (f) $V_{\mathrm{S}0}$, (g) $V_{\mathrm{hor,P}}$, and (h) $V_{\mathrm{nmo,P}}$.
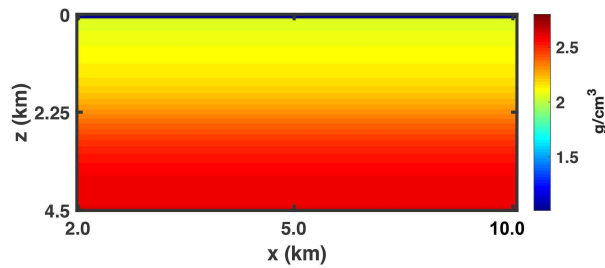
Figure 4. Initial density model for FWI generated using equation 9.

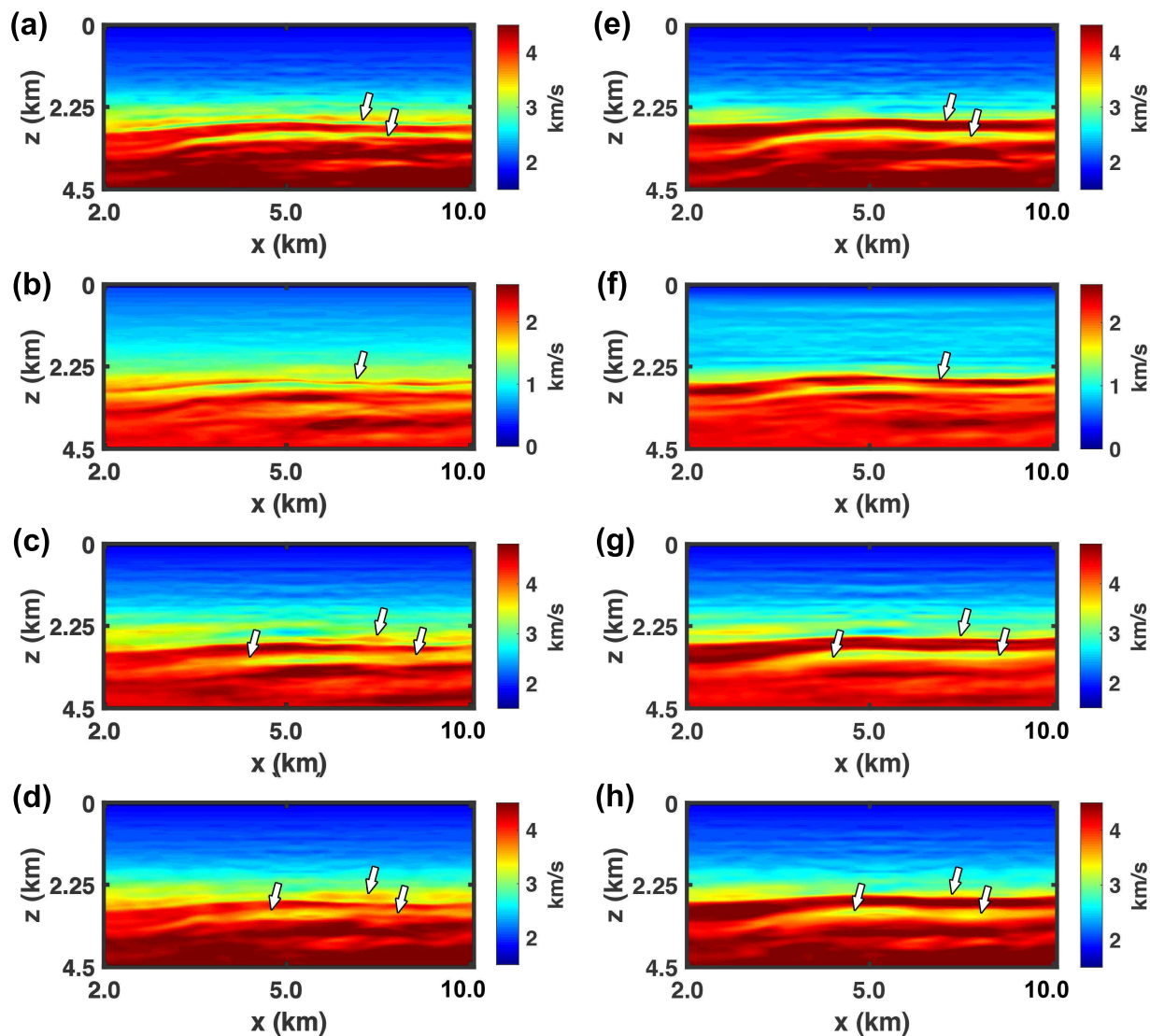**Figure 5.** Results of the unconstrained FWI: (a) V_{P0}, (b) V_{S0}, (c) $V_{hor,P}$, and (d) $V_{nmo,P}$. Results of the facies-based FWI: (e) V_{P0}, (f) V_{S0}, (g) $V_{hor,P}$, and (h) $V_{nmo,P}$. The arrows point to the areas of improvement achieved by the facies-based algorithm.

(in particular, to $V_{hor,P}$ and V_{S0}). Therefore, it is not surprising that the resolution of the velocity $V_{hor,P}$ is lower than that of V_{P0}. Furthermore, the seal layer that corresponds to the high-velocity zone above the reservoir is not visible in the V_{S0}-field. Also, there are noticeable high-velocity artifacts around $z = 2.5$ km and $x > 6$ km (marked by arrows), possibly due to the trade-offs between V_{S0}, $V_{hor,P}$, and $V_{nmo,P}$ (Kamath and Tsvankin, 2016). Note that these artifacts are not present in the tomography (initial FWI) models.

The inversion also produces a reduction in the density values around z=3.1 km, the region that likely corresponds to the reservoir (Figure 6a). However, we observe a similar decrease in density around z=2.35 km that does not correlate with the inverted velocities. Hence, we assume the latter anomaly to be an artifact caused by the parameter trade-offs in the unconstrained FWI.

Even though the unconstrained FWI helps delineate the reservoir region (including the seal), the results suffer from the parameter crosstalk, which needs to be mitigated to improve the model reconstruction.
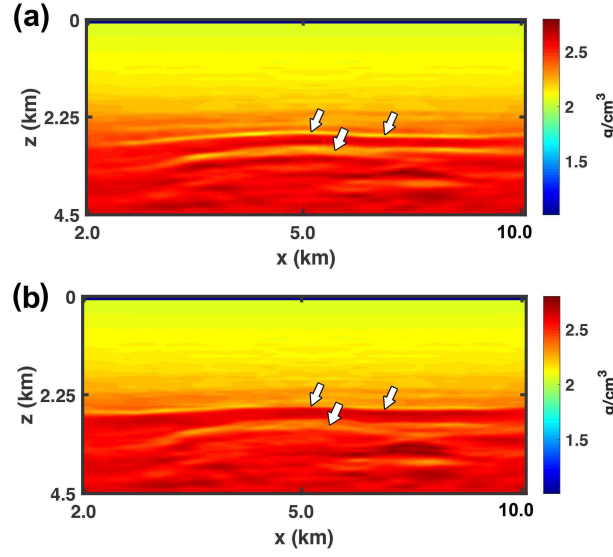
Figure 6. Density inverted using (a) the unconstrained FWI, and (b) the facies-based FWI. The arrows point to the areas of improvement achieved by the facies-based algorithm.

Facies-based FWI

To determine the impact of facies information on the quality of the inversion results, we apply the facies-based FWI algorithm in the same frequency band. The rock-physics constraints for the inversion are computed from the well logs at two borehole locations that provide measurements of V_{P0}, V_{S0}, and ρ (Figure 7). The logs are upscaled prior to FWI to make them suitable for seismic inversion. As shown in Figure 2, the well logs cover a depth interval that includes the reservoir, although the boreholes slightly deviate from the vertical plane that includes the acquisition line. To incorporate the well logs, the borehole measurements are projected onto the vertical acquisition plane at spatial locations of $x = 4.2$ km and $x = 8.2$ km. Because the borehole data are provided as functions of the distance along the well, they are first calibrated to the actual depth before the projection.

Using this borehole information, we build the so-called "depth trend" by assigning sonic and density log values to each facies and horizon to extract the part of the well-log data corresponding to a particular facies. To obtain the facies distribution, we first migrate the data using the imaging condition based on energy norm (Rocha et al., 2017). The migrated image in Figure 8a is obtained by employing the 1D initial TI model; the facies information provided by Equinor is overlaid on that image (Figure 8b). The facies distribution is generally determined from crossplots between different elastic and petrophysical properties. Several machine-learning algorithms have been proposed to generate facies distributions from seismic images in the absence of prior information (Liu et al., 2020; Napoli et al., 2020).

In our case study, we pick a total of eight facies, which align with the major horizons identified in the image. It may be possible to use more advanced classifications of facies and include such important physical parameters as porosity and fluid identifiers.

The next step is to employ image-guided interpolation to compute the spatial distribution of the elastic properties (Zabihi Naeini and Hale, 2016). Because there is no borehole information about the Thomsen coefficients ϵ and δ, these parameters are picked from the tomography models at the borehole locations and combined with the V_{P0}-functions from the well logs to determine $V_{hor,P}$ and $V_{nmo,P}$. The interval velocities $V_{hor,P}$ and $V_{nmo,P}$ near the boreholes can also be obtained from nonhyperbolic moveout inversion of reflection P-wave data (Wang and Tsvankin, 2013; Tsvankin, 2012).

The interpolated models ($\mathbf{m}^{interp}$) and the borehole information are used to assign the best-matched elastic property ($\mathbf{m}^f$) for each facies (Singh et al., 2020b, c):

$$\mathbf{m}^f(i,j) := \min_{n=1...k} \{\mathbf{m}^{interp}(i,j) - \mathbf{D}_T(n)|_{facies(i,j)}\}, \tag{10}$$

where k is the total number of the parameter values in $\mathbf{D}_T$ ("depth trends") that corresponds to a particular facies (Figure 9). Although the accuracy of this procedure would increase if more well logs were available, even sparse prior information improves the convergence of FWI. Because well logs typically cover a limited depth range, it is beneficial to apply facies constraints in the
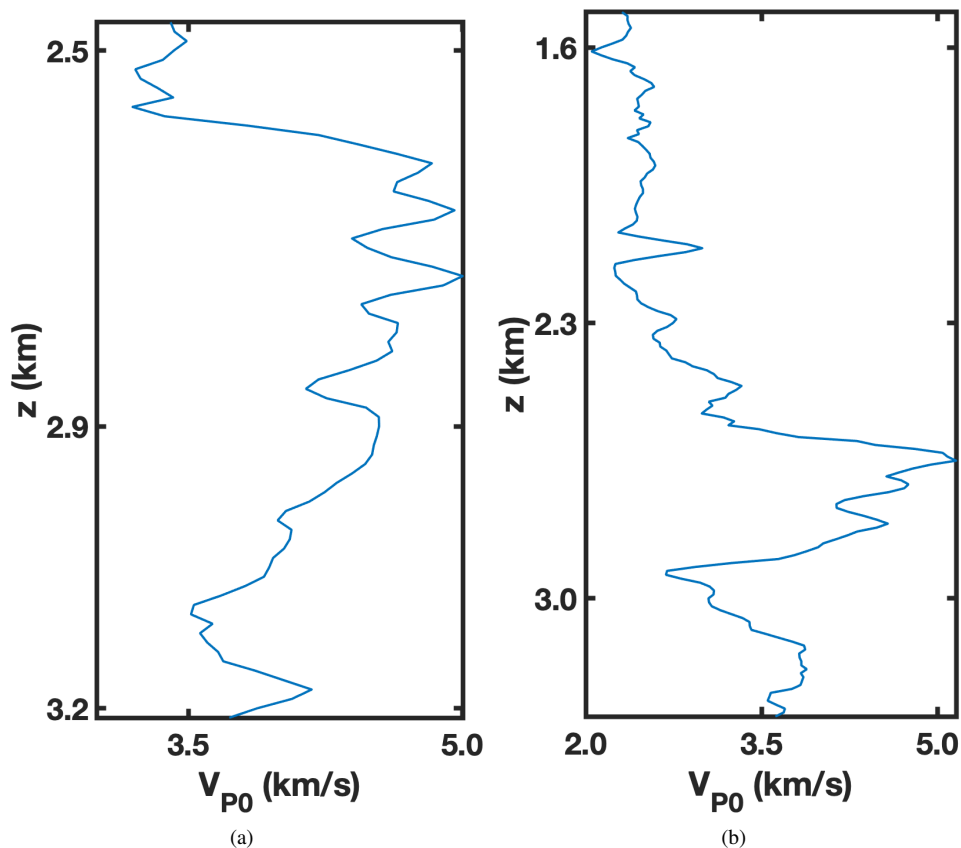
Figure 7. Sonic log profiles of V_{P0} for (a) well 1 (x = 4.5 km) and (b) well 2 (x = 8.2 km).

part of the section where borehole data are available. Therefore, we use a rectangular mask (marked by the rectangle in Figure 9) that covers the area where we preserve facies-based information. This mask acts as the weighting factor $\mathbf{W}_m$ for the model-misfit term in equation 7. This factor is equal to unity inside the rectangle in Figure 9 and decreases exponentially with distance away from that region.

The facies-based FWI reconstructs the model parameters with higher resolution (Figures 5e-h) than the unconstrained FWI (Figures 5a-d). In particular, the issue with the insufficient sensitivity of the vertical-component data to $V_{\mathrm{hor,P}}$ and V_{S0} is substantially mitigated. For example, the seal layer (the high-velocity horizon above the reservoir) is properly reconstructed in the V_{S0}-field (Figure 10). Also, the high-velocity artifacts around $z = 2.5$ km and $x > 6$ km are largely suppressed.

It should be emphasized that density, which is challenging to constrain from surface seismic data, is estimated with higher resolution compared to the unconstrained FWI (Figure 6b). For example, the horizon with a lower density at the top of the plausible reservoir around $z=3.1$ km is better focused, and the likely artifact around $z = 2.35$ km is almost eliminated (Figure 10).

Figure 11 compares seismograms computed for the models estimated by the unconstrained and facies-based inversion with the corresponding field records. Evidently, in addition to increasing parameter resolution, including the facies information reduces the misfit between the observed and simulated data. From Figures 5, 6, 10, and 11 it is clear that the employed lithologic constraints significantly improve the inverted velocity and density fields.

2   DISCUSSION

3D ocean-bottom surveys often provide superior quality of velocity models and seismic images. Full-waveform inversion can be efficiently applied to OBS records because it can operate with multicomponent data and properly handle reflection amplitudes.
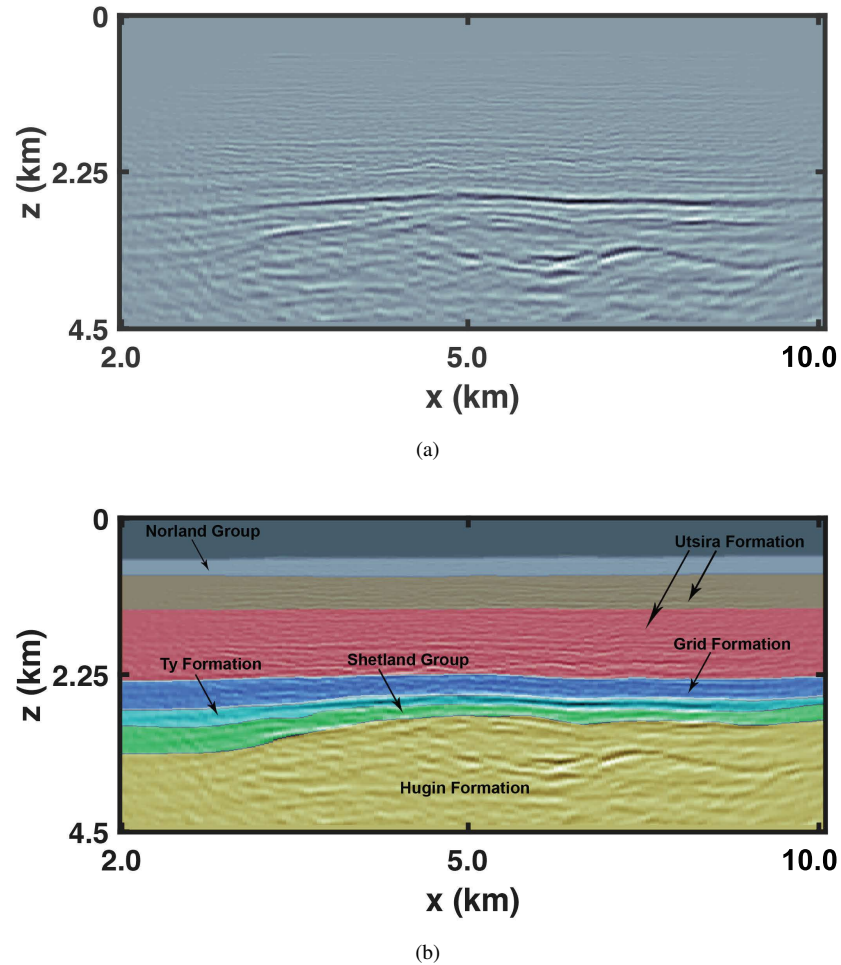
Figure 8. (a) Depth-migrated image obtained using the initial 1D models from Figures 3 and 4. (b) The facies model overlaying plot (a).

However, the signal-to-noise ratio (S/N) on the horizontal particle-velocity components is often too low for their inclusion in FWI, as is the case for the Volve data set.

Hence, here we inverted only the vertical component, which is not sufficiently sensitive to some elastic parameters, such as the shear-wave symmetry-direction velocity V_{S0} and P-wave velocity $V_{hor,P}$. As a result, the unconstrained FWI is unable to adequately reconstruct V_{S0} and $V_{hor,P}$, which is also confirmed by the synthetic tests performed by Singh et al. (2020b). It should be mentioned that simultaneous inversion of the vertical and horizontal components tends to make the objective function more multimodal, which hinders the model-updating procedure (Kamath and Tsvankin, 2016).

The proposed approach that incorporates prior facies information improves the inversion results and increases the parameter resolution in the reservoir region. Borehole data (usually well logs) serve as the primary source of geologic information about the subsurface. The sparseness of the borehole measurements and insufficient information about the reservoir formation in this case study necessitates application of image-guided interpolation with proper spatial weighting.

The facies distribution is generally determined from the correlations between different elastic and petrophysical properties at the borehole locations. In our study, we pick a total of eight facies based on the major horizons in the migrated image and on the available well tops. A more advanced facies classification could include such properties as porosity, shale volume, saturation, etc. Although, several machine-learning (ML) models have been proposed to generate the facies distribution from seismic images (Liu et al., 2020; Li et al., 2020), a model trained on a certain seismic section often becomes inadequate for different geologic settings.

Previous studies that employ reflection tomography show that a tilted TI model provides high-quality images at Volve field (Wang and Tsvankin, 2013). Therefore, we honor the symmetry-axis tilt in the modeling algorithm and continuously update it
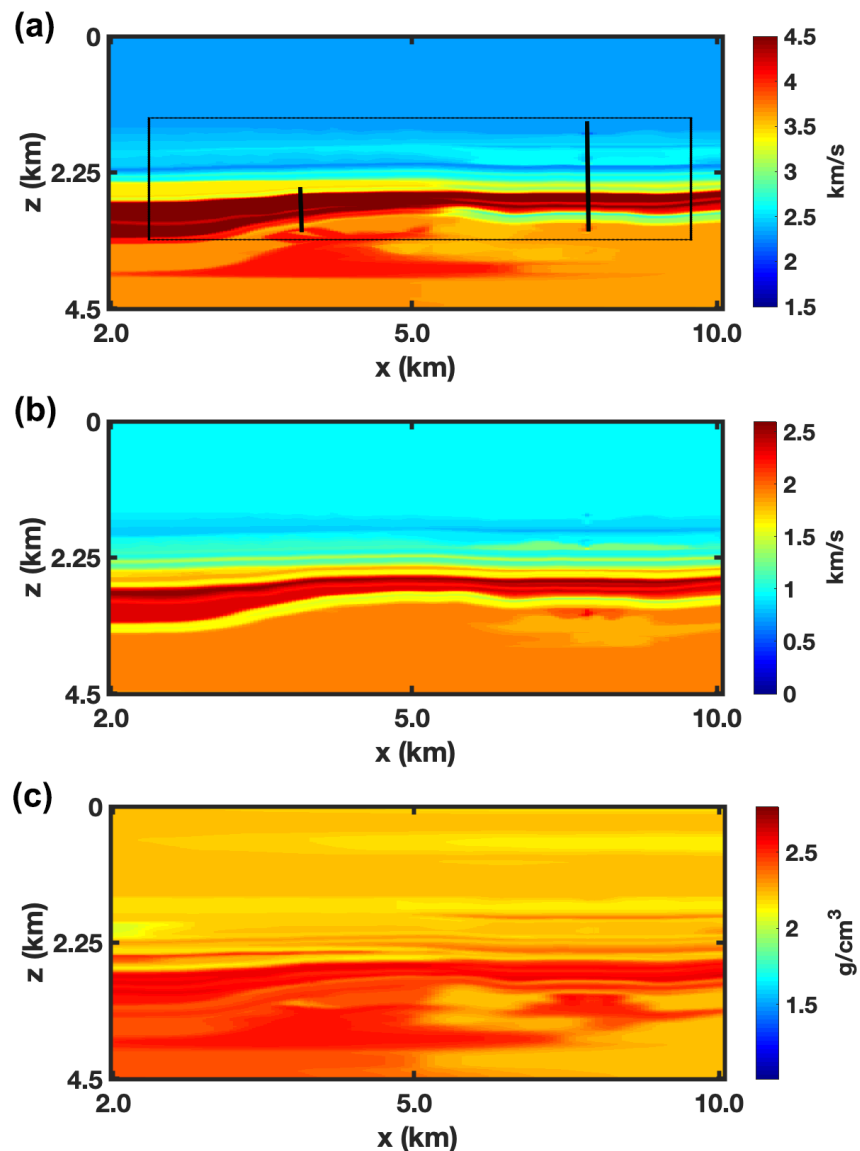
Figure 9. Image-guided interpolated models for (a) V_{P0}, (b) V_{S0}, and (c) ρ obtained using borehole data at the two locations marked by the vertical lines on plot (a). The rectangular mask on plot (a) marks the area where we employ facies-based information.

during the inversion using the imaged structural dips. Although the orientation of the symmetry axis is not estimated by FWI, our results confirm that it is essential to take the symmetry-axis tilt into account.

Zhang and Alkhalifah (2020) show that their facies-based FWI algorithm applied to the same line produces the VTI parameters in the reservoir region with higher resolution compared to the unconstrained inversion. However, the improvement for some of the parameters is marginal, and their unconstrained FWI technique for VTI media does not properly delineate the reservoir. Employing the TTI model improves the results of both unconstrained and facies-based FWI. Also, our methodology increases the resolution for all parameter fields both inside and outside the reservoir. Finally, our algorithm estimates density, which is highly beneficial for both velocity inversion and reservoir characterization.
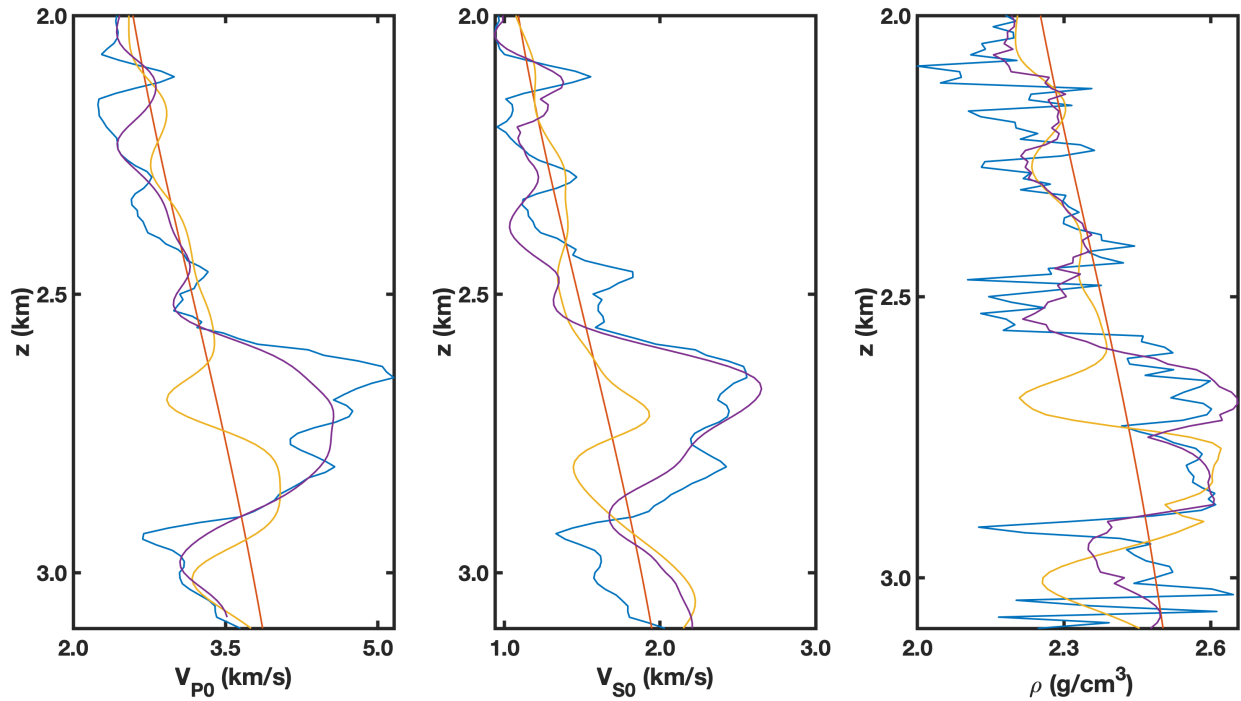
Figure 10. Vertical profiles of V_{P0}, V_{S0}, and ρ at x = 8.2 km. The parameters obtained from the well logs are marked by the blue lines and the initial models by the red lines. The inversion results are marked by the yellow lines (unconstrained FWI) and violet lines (facies-based FWI).

CONCLUSIONS

We applied a modified version of a previously developed facies-based FWI algorithm for anisotropic media to ocean-bottom data from the North Sea. The facies-based constraints obtained from two boreholes mitigate the parameter trade-offs and increase the resolution of the inverted TTI parameters, especially in the reservoir region. The spatial distribution of the facies is built by image-guided interpolation along the major horizons in the depth-migrated image. Then the constraints at each grid point are created by finding the best-matched elastic properties for a given facies. Whereas the facies-based FWI provides better estimates of all medium parameters compared to the unconstrained FWI, the increase in resolution is especially significant for the P-wave velocity in the isotropy plane ($V_{\mathrm{hor,P}}$) and the S-wave symmetry-direction velocity (V_{S0}). It should be emphasized that these improvements are achieved without including low frequencies (0-2 Hz), which were not recorded in this survey. Our algorithm also produces a well-resolved density model, which is a challenging task for FWI of surface reflection data. This case study demonstrates the effectiveness of properly employed geologic constraints in elastic FWI for anisotropic media.
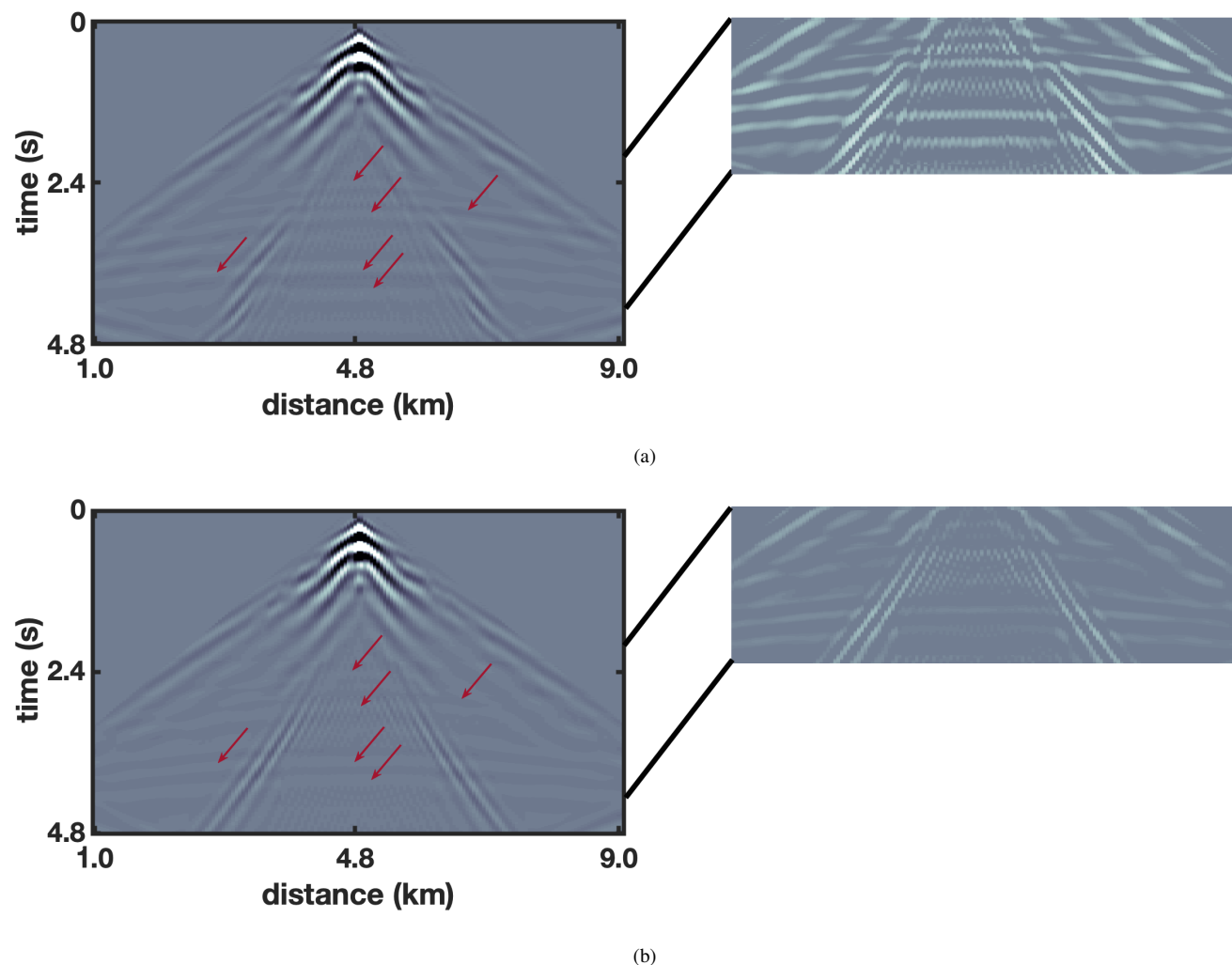
(a)

(b)

Figure 11. Quality of data matching for shot 58 at x ≈ 5 km. The difference between the field record and the seismograms modeled using the output of (a) the unconstrained FWI and (b) the facies-based FWI. The areas of substantial misfit are marked by the arrows. For better visualization, the sections between 2.2 s and 4.6 s are shown at a higher contrast on the right.

4 APPENDIX A

5 STIFFNESS COEFFICIENTS FOR 2D TTI MEDIA

We consider wave propagation in the vertical symmetry plane of a TTI (transversely isotropic with a tilted symmetry axis) medium that contains the symmetry axis. The signatures of P- and SV-waves in that plane are controlled by the P- and S-wave symmetry-direction velocities (V_{P0} and V_{S0}), the P-wave velocity in the isotropy plane ($V_{hor,P} = V_{P0}\sqrt{1+2\epsilon}$), the velocity $V_{nmo,P} = V_{P0}\sqrt{1+2\delta}$, the tilt θ of the symmetry axis with respect to the vertical, and the density (ρ).

The stiffness coefficients in the coordinate system for which the symmetry axis points in the z-direction (i.e., VTI) can be expressed through the velocities and density as follows:

$$c_{11} = \rho\, V_{hor,P}^2 \,,$$

(A-1)

$$c_{13} = \rho \left\{ \sqrt{\left[V_{\text{P0}}^2 - V_{\text{S0}}^2\right]\left[V_{\text{nmo}}^2 - V_{\text{S0}}^2\right]} - V_{\text{S0}}^2 \right\}, \qquad \text{(A-2)}$$

$$c_{33} = \rho\, V_{\text{P0}}^2\,, \qquad \text{(A-3)}$$

$$c_{44} = \rho\, V_{\text{S0}}^2\,, \qquad \text{(A-4)}$$

The 2D equation of motion for P- and SV-waves (equation 2) can be written in the vertical symmetry plane of TTI media as:

$$\begin{aligned}
\rho \frac{\partial v_x}{\partial t} &= \frac{\partial \sigma_{xx}}{\partial x} + \frac{\partial \sigma_{xz}}{\partial z} + f_x\,, \\
\rho \frac{\partial v_z}{\partial t} &= \frac{\partial \sigma_{zz}}{\partial z} + \frac{\partial \sigma_{xz}}{\partial x} + f_z\,, \\
\frac{\partial \sigma_{xx}}{\partial t} &= d_{11}\frac{\partial v_x}{\partial x} + d_{13}\frac{\partial v_z}{\partial z} + d_{15}\left(\frac{\partial v_x}{\partial z} + \frac{\partial v_z}{\partial x}\right), \\
\frac{\partial \sigma_{zz}}{\partial t} &= d_{13}\frac{\partial v_x}{\partial x} + d_{33}\frac{\partial v_z}{\partial z} + d_{35}\left(\frac{\partial v_x}{\partial z} + \frac{\partial v_z}{\partial x}\right), \\
\frac{\partial \sigma_{xz}}{\partial t} &= d_{15}\frac{\partial v_x}{\partial x} + d_{35}\frac{\partial v_z}{\partial z} + d_{55}\left(\frac{\partial v_x}{\partial z} + \frac{\partial v_z}{\partial x}\right),
\end{aligned} \qquad \text{(A-5)}$$

where **v** is the particle velocity and d_{ijkl} is the stiffness tensor. To express the stiffnesses d_{ijkl} through those for the corresponding VTI medium, the axis z has to be rotated by the angle θ. In the two-index (Voigt) notation, the pertinent the stiffnesses d_{ij} are (e.g., Behera, 2017):

$$d_{11} = (c_{11}\cos^2\theta + c_{13}\sin^2\theta)\cos^2\theta + (c_{13}\cos^2\theta + c_{33}\sin^2\theta)\sin^2\theta + 4c_{44}\cos^2\theta\sin^2\theta, \qquad \text{(A-6)}$$

$$d_{13} = c_{11}\cos^2\theta\sin^2\theta + c_{13}\left(\sin^4\theta + \cos^4\theta\right) + c_{33}\cos^2\theta\sin^2\theta - 4c_{44}\cos^2\theta\sin^2\theta, \qquad \text{(A-7)}$$

$$d_{15} = (c_{13} - c_{11})\cos^3\theta\sin\theta + (c_{33} - c_{13})\cos\theta\sin^3\theta + 2c_{44}\cos\theta\sin\theta\left(\cos^2\theta - \sin^2\theta\right), \qquad \text{(A-8)}$$

$$d_{33} = (c_{11}\sin^2\theta + c_{13}\cos^2\theta)\sin^2\theta + (c_{33}\cos^2\theta + c_{13}\sin^2\theta)\cos^2\theta + 4c_{44}\cos^2\theta\sin^2\theta, \qquad \text{(A-9)}$$

$$d_{35} = (c_{13} - c_{11})\cos\theta\sin^3\theta + (c_{33} - c_{13})\cos^3\theta\sin\theta - 2c_{44}\cos\theta\sin\theta\left(\cos^2\theta - \sin^2\theta\right), \qquad \text{(A-10)}$$

$$d_{55} = c_{44}\left(1 - 2\sin^2\theta\right)^2 + (c_{33} - c_{13})\sin^2\theta\cos^2\theta - (c_{13} - c_{11})\sin^2\theta\cos^2\theta. \qquad \text{(A-11)}$$

6 APPENDIX B

7 FWI GRADIENTS FOR 2D TTI MEDIA

The gradient of the objective function (equation 1) for arbitrarily anisotropic media is given by (e.g., Li et al., 2017):

$$\frac{\partial \text{E}_{\text{d}}}{\partial m_n} = -\sum_{ijkl} \frac{\partial d_{ijkl}}{\partial m_n}\left(\int_0^T \frac{\partial u_i}{\partial x_j}\frac{\partial \text{q}_k}{\partial x_l}\right), \qquad \text{(B-1)}$$

where in 2D the indices $i, j, k, l = 1, 2$, T is the total time of wave propagation, **u** and **q** are the forward- and back-propagated displacement fields, respectively, and the vector **m** includes the model parameters (in our case, $m_1 = V_{\text{P0}}$, $m_2 = V_{\text{S0}}$, $m_3 = V_{\text{hor,P}}$, $m_4 = V_{\text{nmo,P}}$, and $m_5 = \rho$).

Kamath and Tsvankin (2016) derive essentially the same expression (equation B-1) for VTI media using the l^2-norm objective function. The only difference is that here the back-propagated wavefield **q** is derived using equation 1; also, we employ the stiffness tensor d_{ijkl} for TTI media.

The derivatives of the objective function (equation B-1) with respect to the TTI parameters are:

$$
\begin{aligned}
\frac{\partial E_{\mathrm{d}}}{\partial V_{\mathrm{P0}}} = -\rho V_{\mathrm{P0}} \int_0^T \Bigg\{ & \frac{\partial q_x}{\partial x}\frac{\partial u_x}{\partial x} d_{11,V_{\mathrm{P0}}} \\
& + \left(\frac{\partial q_x}{\partial x}\frac{\partial u_x}{\partial x} + \frac{\partial q_z}{\partial z}\frac{\partial u_z}{\partial z} \right) d_{13,V_{\mathrm{P0}}} \\
& + \left[\frac{\partial q_x}{\partial x}\left(\frac{\partial u_x}{\partial z} + \frac{\partial u_z}{\partial x} \right) + \left(\frac{\partial q_x}{\partial z} + \frac{\partial q_z}{\partial x} \right)\frac{\partial u_x}{\partial x} \right] d_{15,V_{\mathrm{P0}}} \\
& + \frac{\partial q_z}{\partial z}\frac{\partial u_z}{\partial z} d_{33,V_{\mathrm{P0}}} \\
& + \left[\frac{\partial q_z}{\partial z}\left(\frac{\partial u_x}{\partial z} + \frac{\partial u_z}{\partial x} \right) + \left(\frac{\partial q_x}{\partial z} + \frac{\partial q_z}{\partial x} \right)\frac{\partial u_z}{\partial z} \right] d_{35,V_{\mathrm{P0}}} \\
& + \left(\frac{\partial q_x}{\partial z} + \frac{\partial q_z}{\partial x} \right)\left(\frac{\partial u_x}{\partial z} + \frac{\partial u_z}{\partial x} \right) d_{55,V_{\mathrm{P0}}} \Bigg\} dt \ ,
\end{aligned} \tag{B-2}
$$

$$
\begin{aligned}
\frac{\partial E_{\mathrm{d}}}{\partial V_{\mathrm{S0}}} = -\rho V_{\mathrm{S0}} \int_0^T \Bigg\{ & \frac{\partial q_x}{\partial x}\frac{\partial u_x}{\partial x} d_{11,V_{\mathrm{S0}}} \\
& + \left(\frac{\partial q_x}{\partial x}\frac{\partial u_x}{\partial x} + \frac{\partial q_z}{\partial z}\frac{\partial u_z}{\partial z} \right) d_{13,V_{\mathrm{S0}}} \\
& + \left[\frac{\partial q_x}{\partial x}\left(\frac{\partial u_x}{\partial z} + \frac{\partial u_z}{\partial x} \right) + \left(\frac{\partial q_x}{\partial z} + \frac{\partial q_z}{\partial x} \right)\frac{\partial u_x}{\partial x} \right] d_{15,V_{\mathrm{S0}}} \\
& + \frac{\partial q_z}{\partial z}\frac{\partial u_z}{\partial z} d_{33,V_{\mathrm{S0}}} \\
& + \left[\frac{\partial q_z}{\partial z}\left(\frac{\partial u_x}{\partial z} + \frac{\partial u_z}{\partial x} \right) + \left(\frac{\partial q_x}{\partial z} + \frac{\partial q_z}{\partial x} \right)\frac{\partial u_z}{\partial z} \right] d_{35,V_{\mathrm{S0}}} \\
& + \left(\frac{\partial q_x}{\partial z} + \frac{\partial q_z}{\partial x} \right)\left(\frac{\partial u_x}{\partial z} + \frac{\partial u_z}{\partial x} \right) d_{55,V_{\mathrm{S0}}} \Bigg\} dt \ ,
\end{aligned} \tag{B-3}
$$

$$
\begin{aligned}
\frac{\partial E_{\mathrm{d}}}{\partial V_{\mathrm{hor,P}}} = -\rho V_{\mathrm{hor,P}} \int_0^T \Bigg\{ & \frac{\partial q_x}{\partial x}\frac{\partial u_x}{\partial x} d_{11,V_{\mathrm{hor,P}}} \\
& + \left(\frac{\partial q_x}{\partial x}\frac{\partial u_x}{\partial x} + \frac{\partial q_z}{\partial z}\frac{\partial u_z}{\partial z} \right) d_{13,V_{\mathrm{hor,P}}} \\
& + \left[\frac{\partial q_x}{\partial x}\left(\frac{\partial u_x}{\partial z} + \frac{\partial u_z}{\partial x} \right) + \left(\frac{\partial q_x}{\partial z} + \frac{\partial q_z}{\partial x} \right)\frac{\partial u_x}{\partial x} \right] d_{15,V_{\mathrm{hor,P}}} \\
& + \frac{\partial q_z}{\partial z}\frac{\partial u_z}{\partial z} d_{33,V_{\mathrm{hor,P}}} \\
& + \left[\frac{\partial q_z}{\partial z}\left(\frac{\partial u_x}{\partial z} + \frac{\partial u_z}{\partial x} \right) + \left(\frac{\partial q_x}{\partial z} + \frac{\partial q_z}{\partial x} \right)\frac{\partial u_z}{\partial z} \right] d_{35,V_{\mathrm{hor,P}}} \\
& + \left(\frac{\partial q_x}{\partial z} + \frac{\partial q_z}{\partial x} \right)\left(\frac{\partial u_x}{\partial z} + \frac{\partial u_z}{\partial x} \right) d_{55,V_{\mathrm{hor,P}}} \Bigg\} dt \ ,
\end{aligned} \tag{B-4}
$$

$$
\begin{aligned}
\frac{\partial E_{\mathrm{d}}}{\partial V_{\mathrm{nmo,P}}} = -\rho V_{\mathrm{nmo,P}} \int_0^T \Bigg\{ & \frac{\partial q_x}{\partial x}\frac{\partial u_x}{\partial x} d_{11,V_{\mathrm{nmo,P}}} \\
& + \left(\frac{\partial q_x}{\partial x}\frac{\partial u_x}{\partial x} + \frac{\partial q_z}{\partial z}\frac{\partial u_z}{\partial z} \right) d_{13,V_{\mathrm{nmo,P}}} \\
& + \left[\frac{\partial q_x}{\partial x}\left(\frac{\partial u_x}{\partial z} + \frac{\partial u_z}{\partial x} \right) + \left(\frac{\partial q_x}{\partial z} + \frac{\partial q_z}{\partial x} \right)\frac{\partial u_x}{\partial x} \right] d_{15,V_{\mathrm{nmo,P}}} \\
& + \frac{\partial q_z}{\partial z}\frac{\partial u_z}{\partial z} d_{33,V_{\mathrm{nmo,P}}} \\
& + \left[\frac{\partial q_z}{\partial z}\left(\frac{\partial u_x}{\partial z} + \frac{\partial u_z}{\partial x} \right) + \left(\frac{\partial q_x}{\partial z} + \frac{\partial q_z}{\partial x} \right)\frac{\partial u_z}{\partial z} \right] d_{35,V_{\mathrm{nmo,P}}} \\
& + \left(\frac{\partial q_x}{\partial z} + \frac{\partial q_z}{\partial x} \right)\left(\frac{\partial u_x}{\partial z} + \frac{\partial u_z}{\partial x} \right) d_{55,V_{\mathrm{nmo,P}}} \Bigg\} dt \ .
\end{aligned} \tag{B-5}
$$

The gradient for density can be obtained by applying the chain rule to equation B-1:

$$\begin{aligned}
\frac{\partial E_{\mathrm{d}}}{\partial \rho} = -\int_0^T \bigg\{ &\frac{\partial q_x}{\partial x}\frac{\partial u_x}{\partial x} d_{11,\rho} \\
&+ \left(\frac{\partial q_x}{\partial x}\frac{\partial u_x}{\partial x} + \frac{\partial q_z}{\partial z}\frac{\partial u_z}{\partial z}\right) d_{13,\rho} \\
&+ \left[\frac{\partial q_x}{\partial x}\left(\frac{\partial u_x}{\partial z} + \frac{\partial u_z}{\partial x}\right) + \left(\frac{\partial q_x}{\partial z} + \frac{\partial q_z}{\partial x}\right)\frac{\partial u_x}{\partial x}\right] d_{15,\rho} \\
&+ \frac{\partial q_z}{\partial z}\frac{\partial u_z}{\partial z} d_{33,\rho} \\
&+ \left[\frac{\partial q_z}{\partial z}\left(\frac{\partial u_x}{\partial z} + \frac{\partial u_z}{\partial x}\right) + \left(\frac{\partial q_x}{\partial z} + \frac{\partial q_z}{\partial x}\right)\frac{\partial u_z}{\partial z}\right] d_{35,\rho} \\
&+ \left(\frac{\partial q_x}{\partial z} + \frac{\partial q_z}{\partial x}\right)\left(\frac{\partial u_x}{\partial z} + \frac{\partial u_z}{\partial x}\right) d_{55,\rho} \\
&+ v_x q_x + v_z q_z \bigg\} dt \ .
\end{aligned} \tag{B-6}$$

Here $\boldsymbol{v}$ and $\boldsymbol{q}$ are the forward- and back-propagated particle-velocity fields, respectively. In equations B-2 - B-6, $d_{ijkl,m}$ is the derivative of d_{ijkl} (equations A-6 - A-11) with respect to the model parameter m. For example, $d_{11,V_{\mathrm{P0}}}$ is given by:

$$d_{11,V_{\mathrm{P0}}} = \frac{\partial d_{11}}{\partial V_{\mathrm{P0}}} = \rho\, V_{\mathrm{P0}} \Big\{ 2\sin^2\theta \left(q\cos^2\theta + 2\sin^2\theta\right) \Big\} \ , \tag{B-7}$$

where

$$q = \sqrt{\frac{V_{\mathrm{nmo,P}}^2 - V_{\mathrm{S0}}^2}{V_{\mathrm{P0}}^2 - V_{\mathrm{S0}}^2}} \ .$$

REFERENCES

Alkhalifah T. and R.-E. Plessix, 2014, A recipe for practical full-waveform inversion in anisotropic media: An analytical parameter resolution study: Geophysics, **79**, no. 3, R91–R101.

Asnaashari, A., R. Brossier, S. Garambois, F. Audebert, P. Thore, and J.Virieux, 2013, Regularized seismic full waveform inversion with priormodel information: Geophysics, **78**, no. 2, R25–R36.

Behera, L., 2017, Elastic anisotropic finite-difference full-wave modeling and imaging of the tilted transversely isotropic (TTI) media: 87th Annual International Meeting, SEG, 299-304.

Brossier, R., S. Operto, J. Virieux, 2009. Seismic imaging of complex onshore structures by 2D elastic frequency-domain full-waveform inversion: Geophysics, **74**, 6, WCC105–WCC118.

Dutta, G., M. Sinha, and G. T. Schuster, 2014, A crosscorrelation objective function for least-squares migration and visco-acoustic imaging: 84th Annual International Meeting, SEG, 3985–3990.

Choi, Y., and T. Alkhalifah, 2012, Application of multi-source waveform inversion to marine streamer data using the global correlation norm: Geophysical Prospecting, **60**, no. 4, 748–758.

Guitton, A., G. Ayeni, and E. Daz, 2012, Constrained full-waveform inver-sion by model reparameterization: Geophysics, **77**, no. 2, R117–R127.

Jarillo Michel1, O. and I. Tsvankin, 2017, Waveform inversion for microseismic velocity analysis and event location in VTI media: Geophysics, **82**, no. 4, WA95–WA103.

Kamath, N., and I. Tsvankin, 2016, Elastic full-waveform inversion for VTI media: Methodology and sensitivity analysis: Geophysics, **81**, no. 2, C53–C68.

Li, F., H. Zhou, Z. Wang, and X. Wu, 2021, ADDCNN: An Attention-Based Deep Dilated Convolutional Neural Network for Seismic Facies Analysis With Interpretable Spatial–Spectral Maps: IEEE Transactions on Geoscience and Remote Sensing, **59**, no. 2, 1733-1744.

Li, J., W. Pan, and K. Innanen, 2017, Gradient calculation for anisotropic FWI: Geoconvention, 1-5.

Li, Y. E. and L. Demanet, 2016, Full-waveform inversion with extrapolated low-frequency data: Geophysics, **81**, no. 6, R339-R348.

Liu, M., M. Jervis, W. Li, and P. Nivlet, 2020, Seismic facies classification using supervised convolutional neural networks and semisupervised generative adversarial networks: Geophysics, **85**, no. 4, O47-O58.

Martin, G., R. Wiley, and K. J. Marfurt, 2006, Marmousi2: An elastic upgrade for Marmousi: The Leading Edge, **25**, 156–166.

Napoli, O. O., and V. Martins do Rosario, J. P. Navarro, P. M. C. Silva, and E. Borin, 2020, Accelerating Multi-attribute Unsupervised Seismic Facies Analysis With RAPIDS: ArXiv, abs/2007.15152.

Oh, J-W., Y. Shin, T. Alkhalifah, D-J. Min, 2020, Multistage elastic full-waveform inversion for tilted transverse isotropic media: Geophysical journal international, **223**, no. 1, 57-76.

Operto, S., Y. Gholami, V. Prieux, A. Ribodetti, R. Brossier, L. Metivier, andJ. Virieux, 2013, A guided tour of multiparameter full waveform inversionwith multicomponent data: From theory to practice: The Leading Edge, **32**, no. 9, 1040–1054.

Pan, W., K. A. Innanen, G. F. Margrave, M. C. Fehler, X. Fang, and J. Li,2016, Estimation of elastic constants for HTI media using Gauss-Newton and full-Newton multiparameter full-waveform inversion: Geophysics, **81**, no. 5, R275–R291.

Pratt, R. G., B. Smithyman, 2018. Full waveform inversion for density: reciprocity, divergence, parameter resolution, and other issues: 80th EAGE Conference and Exhibition, 1-5.

Plessix, R.-E. and W. A. Mulder, 2004, Frequency-domain finite-difference amplitude-preserving migration: Geophysical Journal International, **157**, no. 3, 975–987, doi: 10.1111/j.1365-246X.2004.02282.x.

Qu, Y., Z. Li, J. Huang, 2017, Elastic full-waveform inversion for surface topography: Geophysics, **82**, no. 5, R269–R285.

Rocha, D., N. Tanushev, and P. Sava, 2017, Anisotropic elastic wavefield imaging using the energy norm: Geophysics, **82**, no. 3, S225–S234.

Shipp, R. M. and S. C. Singh, 2002. Two-dimensional full wavefield inversion of wide-aperture marine seismic streamer data: Geophysical Journal International, **151**, no. 2, 325–344.

Singh, S., I. Tsvankin, and E. Zabihi Naeini, 2018, Bayesian framework for elastic full-waveform inversion with facies information: The Leading Edge, **37**, no. 12, 924-931.

Singh, S., I. Tsvankin, and E. Zabihi Naeini, 2020a, Elastic full-waveform inversion with geologic information for tilted TI media: 82nd Annual Conference and Exhibition, EAGE, 1-5.

Singh, S., I. Tsvankin, and E. Zabihi Naeini, 2020b, Full-waveform inversion for elastic VTI media with borehole constraints: Geophysics, **85**, no. 6, R553–R563.

Singh, S., I. Tsvankin, and E. Zabihi Naeini, 2021, Elastic FWI for orthorhombic media with lithologic constraints applied via machine learning, Geophysics (under review).

Singh, S., and I. Tsvankin, 2021, Sensitivity analysis of elastic full-waveform inversion for orthorhombic media, Geophysics (under review).

Szydlik, T., P. Smith, S. Way, L. Aamodt, and C. Friedrich, 2007, 3D PP/PS prestack depth migration on the Volve field: First Break, **25**, no. 4, 43–47.

Tarantola, A., 1984, Inversion of seismic reflectiondata in the acoustic approximation: Geophysics, **49**, no. 8, 1259–1266.

Tsvankin, I. and V. Grechka, 2011, Seismology of azimuthally anisotropic media and seismic fracture characterization: Society of Exploration Geophysicists.

Tsvankin, I., 2012, Seismic signatures and analysis of reflection data in anisotropic media: 3rd ed., Society of Exploration Geophysicists.

Wang, X., and I. Tsvankin, 2013, Multiparameter TTI tomography of P-wave reflection and VSP data: Geophysics, **78**, no. 5, WC51-WC63.

Wu, R., J. Luo, and B. Wu, 2014, Seismic envelope inversion and modulation signal model: Geophysics, **79**, no. 3, WA13–WA24.

Zabihi Naeini, E., and D. Hale, 2015, Image- and horizon-guided interpo-lation: Geophysics, **80**, no. 3, V47–V56.

Zhang, Z., T. Alkhalifah, E. Zabihi Naeini, and B. Sun, 2018, Multiparameter elastic full waveform inversion with facies-based constraints: Geophysical Journal International, **213**, no. 3, 2112-2127.

Zhang, Z., T. Alkhalifah, 2019, Regularized elastic full-waveform inversion using deep learning: Geophysics, **84**, no. 5, R741–R751.

Zhang, Z., T. Alkhalifah, 2020, High-resolution reservoir characterization using deep learning-aided elastic full-waveform inversion: The North Sea field data example, Geophysics, **85**, no. 4, WA137-WA146.